

# Hard exclusive meson production in muon scattering at COMPASS

Andrzej Sandacz<sup>1,\*,\*\*</sup>, on behalf of the COMPASS Collaboration

<sup>1</sup>National Institute for Nuclear Research, Division of High Energy Physics,  
ul. Pasteura 7 Warsaw, PL 02-093, Poland

**Abstract.** We report on measurements of hard exclusive muoproduction of  $\rho^0$ ,  $\omega$  and  $\pi^0$  mesons on the proton at COMPASS using 160 GeV/c polarized  $\mu^+$  and  $\mu^-$  beams scattering off a liquid hydrogen target. The extracted Spin Density Matrix Elements for vector mesons indicate a violation of  $s$ -channel helicity conservation for transitions of transversely polarized virtual photons to longitudinally polarized vector mesons,  $\gamma_T \rightarrow V_L$ , where  $V$  denotes  $\rho^0$  or  $\omega$  meson. Additionally, for  $\rho^0$  production we observe a dominant contribution of natural-parity-exchange transitions and a small contribution of unnatural-parity-exchange transitions. On the contrary, the contribution of unnatural-parity-exchange for  $\omega$  production is significant and it decreases with increasing  $W$ , being still non-negligible at the largest  $W$  values accessible at COMPASS. Further, we present also the absolute value of the differential cross section for exclusive  $\pi^0$  production and its dependence on squared four-momentum transfer  $t$  and azimuthal angle  $\phi$  between the scattering plane and  $\pi^0$  production plane. The results provide an important input for modeling Generalized Parton Distribution (GPDs), and in particular to constrain chiral-odd (transversity) GPDs.

## 1 Introduction

Exclusive meson production in lepton-nucleon scattering is a convenient tool for studying the production mechanism and, in a model-dependent way, the structure of the nucleon. Such process is an important tool to access Generalised Parton Distributions (GPDs) [1–3]. The theoretical framework of GPDs offers a novel description of the nucleon’s partonic structure and contain a wealth of new information. The GPDs provide a description of the nucleon as an extended object, sometimes referred to as a 3-dimensional ‘nucleon tomography’ [4], which correlates transverse spatial and longitudinal momentum degrees of freedom. The GPDs also allow access to such a fundamental property of the nucleon as the orbital angular momentum of quarks [2]. The mapping of the nucleon GPDs requires a comprehensive program of measuring various hard processes in a broad kinematic range, in particular Hard Exclusive Meson Production (HEMP).

The phenomenological GPD model that presently provides predictions for all types of experimental observables is the one of Goloskokov and Kroll [5–7] (GK model). It is a so-called handbag model that contains terms beyond the collinear factorization, which was

\*Work supported by the Polish NCN Grant 2020/37/B/ST2/01547.

\*\*e-mail: [andrzej.sandacz@ncbj.gov.pl](mailto:andrzej.sandacz@ncbj.gov.pl)

proven rigorously only for longitudinally polarized virtual photons. The model is applicable for a comparison with results of existing measurements, also without transverse vs. longitudinal separation.

## 2 Experimental set-up

The data used for this analysis were recorded in 2012 during a four weeks pilot run for the COMPASS GPD program. COMPASS is a fixed-target experiment situated at the high-intensity M2 beam-line of the CERN SPS. It can deliver either hadron or naturally polarised muon beams of a given charge in the energy range between 50 and 280 GeV. For the GPD program the data are collected with the muon beam nominal energy of 160 GeV and with muons of both polarities:  $\mu^+$  ( $\mu^-$ ) with polarisation of about -0.8 (+0.8).

The COMPASS apparatus [8] consists of a two-stage forward spectrometer comprising various tracking detectors, electromagnetic and hadronic calorimeters, muon identification detectors, and a ring imaging Cherenkov counter grouped around two dipole magnets SM1 and SM2. For the GPD program the set-up was complemented by installing the recoil proton detector CAMERA around the 2.5 m long liquid hydrogen target and the large-angle electromagnetic calorimeter ECAL0. The recoil proton detection is based on the ToF measurement. The calorimeter ECAL0 that is situated just downstream of CAMERA allows to extend the accessible kinematic domain for Deeply Virtual Compton Scattering and exclusive  $\pi^0$  production towards higher values of Bjorken  $x_{Bj}$  and to improve hermeticity for detection of exclusive events. By adding these detectors COMPASS has been converted into a facility measuring exclusive reactions within kinematic domain from  $x \sim 0.01$  to  $\sim 0.15$ , which cannot be explored at any other existing or planned facility in the near future.

## 3 Results on exclusive vector meson production

### 3.1 Selections of events from exclusive vector meson production

In the following we present in more detail selections of events for  $\rho^0$  data, which are preliminary, while analogous selections for published  $\omega$  results can be found in Ref. [9]. An event to be accepted for the analysis is required to have an incident muon track, a scattered muon track and only two hadron tracks with opposite charges. Most of other applied event selections are either the same or similar to those used for the published COMPASS results on Spin Density Matrix Elements (SDMEs) for exclusive  $\omega$  production [9]. As the recoil proton detector restricts the kinematic coverage towards low momentum transfers, it was not used in this analysis. Instead, in order to enhance the fraction of events with exclusively produced  $\rho^0$  mesons, the missing energy

$$E_{\text{miss}} = \frac{M_X^2 - M^2}{2M} \quad (1)$$

is constrained by  $-2.5 \text{ GeV} < E_{\text{miss}} < 2.5 \text{ GeV}$  to take into account the experimental resolution. Here,  $M$  is the proton mass,  $M_X^2 = (p + q - p_{\pi^+} - p_{\pi^-})^2$  is the missing mass squared, and  $p$ ,  $q$ ,  $p_{\pi^+}$  and  $p_{\pi^-}$  are the four-momenta of target nucleon, virtual photon and each of two pions.

Selected kinematic distributions are shown in Fig. 1. These are the invariant mass of the  $\pi^+\pi^-$  system and  $E_{\text{miss}}$  distributions. A clear  $\rho^0$  signal is observed. The distribution for the data is compared to the result of the HEPGEN Monte Carlo (MC), which generates only exclusive production of  $\rho^0$  resonance. An observed skewing in the invariant mass distribution for the data with respect to MC is due to a small contribution of exclusive non-resonant pion-pair production and its interference with the resonant production. Within the selected range

$0.5 \text{ GeV}/c^2 < M_{\pi^+\pi^-} < 1.1 \text{ GeV}/c^2$  the contribution from non-resonant production, including the interference term, is equal to about 3% and thus is neglected.

In Fig. 1 (right) the  $E_{\text{miss}}$  distributions for the data and the background, which was evaluated using LEPTO Monte Carlo (MC), are shown. The amount of background in the signal window  $|E_{\text{miss}}| < 2.5 \text{ GeV}$  depends on  $Q^2$ ,  $W$  and  $p_T^2$ , and when averaged over the total kinematic range it amounts to 17%. The background-corrected data are represented by the shaded histogram.

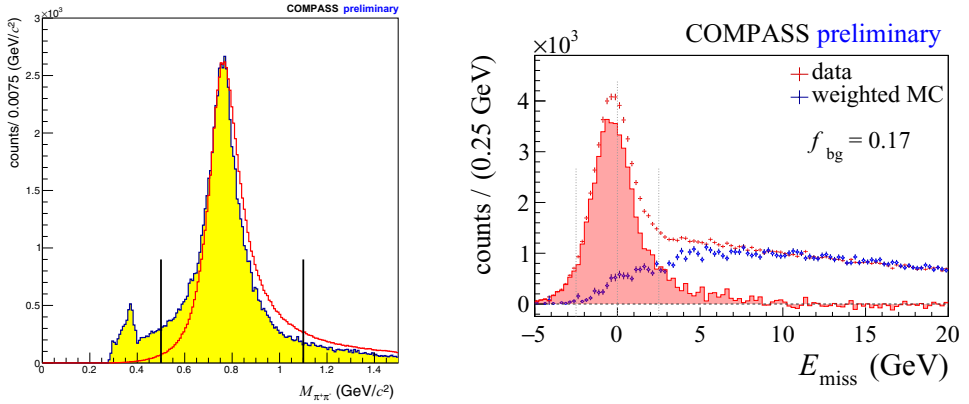


**Figure 1.** **Left:** Distribution of the  $\pi^+\pi^-$  invariant mass for the experimental data (shaded histogram) and for the HEPGEN MC (open histogram). The invariant mass distribution from HEPGEN is normalized to the data in the region  $0.75 \text{ GeV}/c^2 < M_{\pi\pi} < 0.77 \text{ GeV}/c^2$ . The vertical lines indicate the applied limits. **Right:** The missing-energy distribution from experimental data compared to the distribution of SIDIS events from a LEPTO MC simulation. The MC distribution is normalized to the data in the region  $7 \text{ GeV} < E_{\text{miss}} < 20 \text{ GeV}$ . The background-corrected distribution for the data is shown as shaded histogram. The vertical lines at  $|E_{\text{miss}}| = 2.5 \text{ GeV}$  indicate the limits of the exclusive region. Each LEPTO MC event is reweighted by a  $E_{\text{miss}}$ -dependent weight that is calculated using both experimental and simulated data with same-charge hadron pairs.

The selected  $\rho^0$  sample consists of 23785 events for  $\mu^+$  and 28472 for  $\mu^-$  beam. For comparison we quote the published total number of selected events for exclusive  $\omega$  production [9], which is 3060 events. The lower number for the  $\omega$  channel is due to the cross section being about an order of magnitude smaller and a lower acceptance than those for  $\rho^0$  production. The measurements for both channels cover the kinematic region  $5.0 \text{ GeV}/c^2 < W < 17.0 \text{ GeV}/c^2$ ,  $1.0 (\text{GeV}/c)^2 < Q^2 < 10.0 (\text{GeV}/c)^2$  and  $0.01 (\text{GeV}/c)^2 < p_T^2 < 0.5 (\text{GeV}/c)^2$ .

### 3.2 Spin Density Matrix Elements

The vector meson spin density matrix elements are proportional to the bilinear combinations of helicity amplitudes  $F_{\lambda_V \lambda'_N \lambda_\gamma \lambda_N}$  [10]. These amplitudes describe the transition of a virtual photon with helicity  $\lambda_\gamma$  to a vector meson with helicity  $\lambda_V$ , while  $\lambda_N$  and  $\lambda'_N$  are the helicities of the nucleon in the initial and final states, respectively.

The SDMEs can be determined from the fit of three-dimensional angular distribution describing the production and decay of a vector meson to the corresponding experimental distribution. Definitions of angles and reference frames are given in Refs. [9, 11].

SDMEs for exclusive  $\rho^0$  production extracted for the entire kinematic region with  $\langle Q^2 \rangle = 2.4$  (GeV/c)<sup>2</sup>,  $\langle W \rangle = 9.9$  GeV and  $\langle p_T^2 \rangle = 0.18$  (GeV/c)<sup>2</sup> are presented in Fig. 2 (left). These SDMEs are divided into five classes corresponding to different helicity transitions. The main terms in the expressions of SDMEs by helicity amplitudes of class A, correspond to the transitions from longitudinal virtual photons to longitudinal vector mesons,  $\gamma_L^* \rightarrow V_L$ , and from transverse virtual photons to transverse vector mesons,  $\gamma_T^* \rightarrow V_T$ . In class B the dominant terms correspond to the interference of the above two transitions. The main terms of SDMEs in classes C, D and E are proportional to the amplitudes describing  $\gamma_T^* \rightarrow V_L$ ,  $\gamma_L^* \rightarrow V_T$  and  $\gamma_T^* \rightarrow V_{-T}$  transitions, respectively.

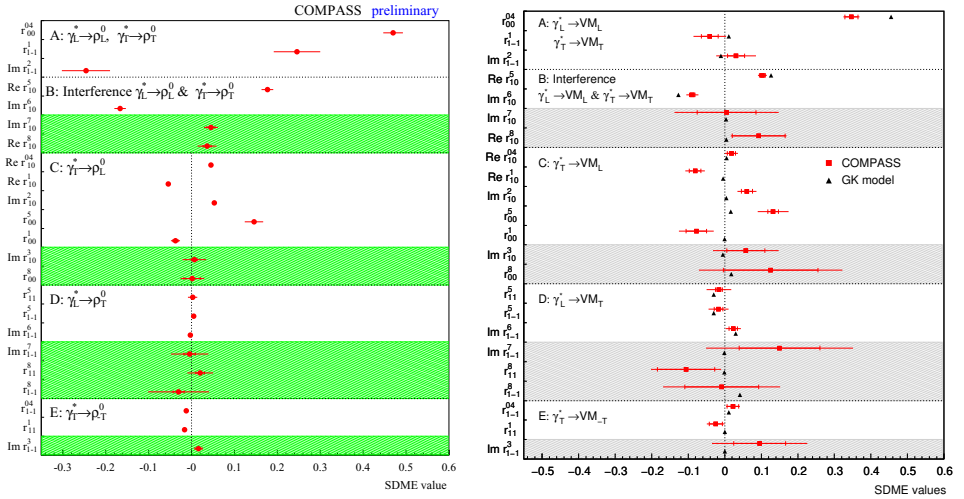


**Figure 2. Left:** The 23 SDMEs for exclusive  $\rho^0$  leptoproduction extracted in the entire COMPASS kinematic region with  $\langle Q^2 \rangle = 2.4$  (GeV/c)<sup>2</sup>,  $\langle W \rangle = 9.9$  GeV/c<sup>2</sup>,  $\langle p_T^2 \rangle = 0.18$  (GeV/c)<sup>2</sup>. The inner error bars represent the statistical uncertainties, while the outer ones indicate the statistical and systematic uncertainties added in quadrature. Unpolarized (polarized) SDMEs are displayed in the unshaded (shaded) areas. **Right:** The measured SDMEs for exclusive  $\omega$  production compared to predictions of the GPD model of Goloskokov and Kroll [7]. The calculations are obtained for  $Q^2 = 2.0$  (GeV/c)<sup>2</sup>,  $W = 7.5$  GeV/c<sup>2</sup> and  $p_T^2 = 0.14$  (GeV/c)<sup>2</sup>.

In case of s-channel helicity conservation (SCHC) only the seven SDMEs of classes A and B may not vanish. However, for the transition  $\gamma_T^* \rightarrow V_L$  (class C) one can observe a clear violation of SCHC. In the GK model [6] the SDMEs from class C are related to the contributions from transversity GPDs  $\bar{E}_T$  and  $H_T$  coupled with the higher-twist wave function of the meson.

The SDME values for exclusive  $\omega$  production [9] for the total kinematic region with mean values  $\langle Q^2 \rangle = 2.13$  (GeV/c)<sup>2</sup>,  $\langle W \rangle = 7.6$  GeV/c<sup>2</sup> and  $\langle p_T^2 \rangle = 0.16$  (GeV/c)<sup>2</sup> are shown in Fig. 2 (right). They are compared to the predictions for COMPASS of the GPD model of Goloskokov and Kroll [6, 7]. The model was tuned to HERMES results on SDMEs and spin asymmetries for exclusive  $\rho^0$  and  $\omega$  production, which led to a satisfactory agreement between the model and the HERMES data.

The most noticeable differences between COMPASS results and the model predictions are following: i) the predicted value of SDME  $r_{00}^{04}$ , which represents the fraction of longitudinally polarized mesons in the produced sample, is significantly larger than the measured one; ii) the SDMEs sensitive to the transitions  $\gamma_T^* \rightarrow \omega_L$  (class C) are in general close to zero in

the model, while in the data several of them ( $r_{00}^5$ ,  $\text{Re}\{r_{10}^1\}$ ) indicate a clear violation of the SCHC hypothesis. As the COMPASS results on SDMEs cover the kinematic range of  $W$  that extends considerably towards higher values of  $W$  compared to HERMES, it is expected that they may help to further constrain the model parameterizations. For constraining models the COMPASS results for the  $\omega$  and  $\rho^0$  channels are complementary. First,  $\omega$  production is sensitive to unnatural parity exchange (UPE) amplitudes with large contribution from pion-pole exchange, while  $\rho^0$  production is predominantly described by natural parity exchange (NPE) amplitudes (see Sec. 3.3). Next, for the helicity-flip NPE amplitudes each of the two channels has a different sensitivity to transversity GPDs  $H_T$  and  $\tilde{E}_T = 2\tilde{H}_T + E_T$ .

### 3.3 Unnatural parity exchange contribution

The existence of UPE transitions in exclusive vector meson production can be tested by examining linear combination of certain SDMEs. The UPE fractional contribution  $\Delta_{\text{UPE}}$  to the cross section for exclusive  $\rho^0$  production at COMPASS is very small. The value of  $\Delta_{\text{UPE}}$  for the entire kinematic range is  $0.024 \pm 0.005 \pm 0.014$ . This is in a sharp contrast with a significant UPE contribution in exclusive  $\omega$  production observed by COMPASS [9] in the same kinematic range. For the latter one the value for the entire kinematic range is equal to  $0.415 \pm 0.037 \pm 0.025$ . For  $\omega$  production the UPE dominates at small  $W$  values and its contribution decreases with increasing  $W$  without vanishing towards the largest  $W$  values accessible in COMPASS. In the GK model, UPE is described by the GPDs  $\tilde{H}^f$  and  $\tilde{E}^f$  (non-pole), and by the pion-pole contribution treated as a one-boson exchange [7]. The difference between UPE for  $\omega$  and  $\rho^0$  is mostly explained by the different  $\pi-\omega$  and  $\pi-\rho^0$  transition form factors, with the former one being about 3 times larger than the latter. The difference comes from different quark-charge contributions in both cases.

Another observable that is sensitive to the relative contributions of UPE and NPE amplitudes is the NPE-to-UPE asymmetry of the transverse differential cross section for the transition  $\gamma_T^* \rightarrow V_T$ . It is defined [7] as

$$P = \frac{2r_{1-1}^1}{1 - r_{00}^{04} - 2r_{1-1}^{04}} \approx \frac{d\sigma_T^N(\gamma_T^* \rightarrow V_T) - d\sigma_T^U(\gamma_T^* \rightarrow V_T)}{d\sigma_T^N(\gamma_T^* \rightarrow V_T) + d\sigma_T^U(\gamma_T^* \rightarrow V_T)}, \quad (2)$$

where the superscripts  $N$  and  $U$  denote the parts of the cross section that are fed by NPE and UPE transitions, respectively.

The value of  $P$  for  $\rho^0$  obtained in the total kinematic region is  $0.887 \pm 0.016 \pm 0.029$ , which indicates that NPE contribution dominates when averaged over the whole kinematic range of COMPASS. The kinematic dependences of the asymmetry  $P$  for  $\rho^0$  are shown in the upper panel of Fig. 3. A possible small UPE contribution is observed only at small values of  $W$  and it becomes compatible with zero at larger  $W$ . No significant  $Q^2$  and  $p_T^2$  dependences of the asymmetry are observed.

The COMPASS results for exclusive  $\omega$  production [9] on the asymmetry  $P$  and its kinematic dependences exhibit a different behaviour as shown in the lower panel of Fig. 3. For the whole kinematic region the value of  $P$  is compatible with zero ( $P = -0.007 \pm 0.076 \pm 0.125$ ), which indicates that the UPE and NPE contributions averaged over the whole kinematic range are of similar size. The UPE contribution dominates at small values of  $W$  and decreases with increasing  $W$ . At large values of  $W$  the NPE contribution becomes dominant, while a non-negligible UPE contribution still remains.

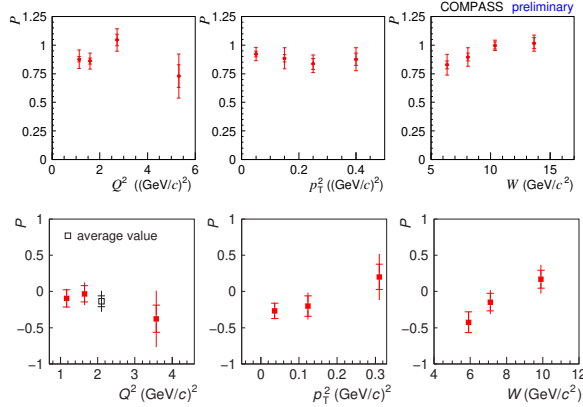


**Figure 3.**  $Q^2$ ,  $p_T^2$  and  $W$  dependences of the NPE-to-UPE asymmetry for transverse cross section for transitions  $\gamma_T^* \rightarrow V_T$  in exclusive  $\rho^0$  production (**top**) and exclusive  $\omega$  production (**bottom**). The inner error bars represent the statistical uncertainties, while the outer ones indicate the statistical and systematic uncertainties added in quadrature.

## 4 Results on exclusive $\pi^0$ production

For the analysis of exclusive  $\pi^0$  production,  $\mu p \rightarrow \mu' p' \pi^0$ , the use of the information from the CAMERA detector was essential. The procedure for event selection, subtraction of non-exclusive background and extraction of the absolute value of the differential cross section is described in Ref. [12]. Here, we only mention briefly that the four-fold differential  $\mu p$  cross sections was extracted separately for  $\mu^+$  and  $\mu^-$  data. Then the unpolarised cross section was obtained as the weighted mean of the two. In this way the dependence on the beam polarisation cancels. In order to convert  $\mu p$  cross section into  $\gamma^* p$  cross section we divide the former one by the transverse virtual photon flux.

The unpolarised  $\gamma^* p$  cross section for exclusive  $\pi^0$  production reads

$$\frac{d^2\sigma^{\gamma^* p}}{dt d\phi} = \frac{1}{2\pi} \left[ \frac{d\sigma_T}{dt} + \epsilon \frac{d\sigma_L}{dt} + \epsilon \cos(2\phi) \frac{d\sigma_{TT}}{dt} + \sqrt{2\epsilon(1+\epsilon)} \cos(\phi) \frac{d\sigma_{LT}}{dt} \right], \quad (3)$$

where  $\sigma_T, \sigma_L, \sigma_{TT}, \sigma_{LT}$  are the structure functions,  $\epsilon$  is the virtual photon polarisation parameter and  $\phi$  represents the azimuthal angle between lepton scattering plane and  $\pi^0$  production plane. Here, the subscript  $T(L)$  denotes the contribution from transversely (longitudinally) polarised virtual photons, while the subscripts  $TT$  and  $LT$  denote the contributions from the interference between transversely-transversely and longitudinally-transversely polarised photons.

After integration over  $\phi$ , we extract the cross section in bins of  $|t|$ , which is displayed in Fig. 4 (left). It decreases exponentially with increasing  $|t|$  at values of  $|t|$  larger than about  $0.25 \text{ (GeV}/c)^2$ , while at smaller  $|t|$  the  $t$ -dependence becomes weaker. Being the first measurement at energies significantly higher than previous results, it is worth to compare it to the model prediction. The COMPASS result is compared to the predictions of the Goloskokov-Kroll model [13, 14]. The dash-dotted and dotted curves represent the cross section from two versions of the model as a function of  $t$ , while the triangles correspond to the cross section averaged over  $|t|$  bins of the data. The mean values of the cross section for the full  $t$ -range are compared at the rightmost part of the plot. We observe that the magnitude of the earlier prediction of the model [13] for the cross section overshoots our measurement by approximately a factor of two.

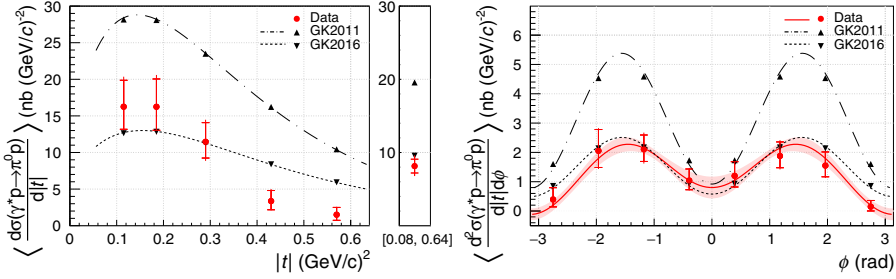


**Figure 4.** **Left:** The exclusive  $\pi^0$  cross section as a function of  $|t|$ . COMPASS results are compared to predictions of the GPD model of Ref. [13, 14]. **Right:** The exclusive  $\pi^0$  cross section as a function of  $\phi$ . Solid line indicates the result of the fit to the data.

Furthermore, we extract the cross section as a function of  $\phi$  in the range of measured  $t$  and eight bins of  $\phi$  of equal width. The dots in Fig. 4 (right) show the measured cross section for each bin and a fit of the function given by Eq. (3), which is represented by the continuous curve. We observe a large contribution from  $\sigma_{TT}$  and a smaller positive one from  $\sigma_{LT}$ . This indicates a significant role of transversely polarised photons in exclusive  $\pi^0$  production.

According to Refs. [13, 15] the structure functions for exclusive pseudo-scalar meson production, which appear in Eq. (3), depend on GPDs  $\tilde{H}^q$ ,  $\tilde{E}^q$ ,  $H_T^q$  and  $\tilde{E}_T^q = 2\tilde{H}_T^q + E_T^q$ . For  $\pi^0$  production a large contribution from transversely polarised virtual photons is expected, which is mainly generated by the chiral-odd ('transversity') GPDs  $\tilde{E}_T^q$ . It manifests itself in a large contribution from  $\sigma_{TT}$  and a dip in the differential cross section  $d\sigma/dt$  as  $|t|$  decreases to zero.

## Acknowledgements

We acknowledge the support by the European Union's Horizon 2020 research and innovation programme under grant agreement STRONG-2020 - No 824093.

## References

- [1] D. Müller et al., Fortschr. Phys. **42**, 101 (1994)
- [2] X. Ji, Phys. Rev. Lett. **78**, 610 (1997); Phys. Rev. D **55**, 7114 (1997)
- [3] A.V. Radyushkin, Phys. Lett. B **385**, 333 (1996); A.V. Radyushkin, Phys. Rev. D **56**, 5524 (1997)
- [4] M. Burkardt, Phys. Rev. D **62** (2000) 071503; erratum-ibid. D **66** (2002) 119903; Int. J. Mod. Phys. A **18** (2003) 173; Phys. Lett. B **595** (2004) 245
- [5] S.V. Goloskokov and P. Kroll, Eur. Phys. J. C **42**, 281 (2005); Eur. Phys. J. C **53**, 367 (2008); Eur. Phys. J. C **59**, 809 (2009)
- [6] S.V. Goloskokov and P. Kroll, Eur. Phys. J. C **74** 2725 (2014)
- [7] S.V. Goloskokov and P. Kroll, Eur. Phys. J. A **50** 146 (2014)
- [8] P. Abbon et al. (COMPASS Collaboration), Nucl. Instr. Meth. A **577** 455 (2007); Nucl. Instr. Meth. A **779** 69 (2015)
- [9] G.D. Alexeev et al. (COMPASS Collaboration), Eur. Phys. J. C **81**, 126 (2021)
- [10] K. Schilling and G. Wolf, Nucl. Phys. B **61**, 381 (1973)
- [11] A. Airapetian et al. (HERMES Collaboration), Eur. Phys. J. C **62**, 659 (2009)
- [12] M.G. Alexeev et al. (COMPASS Collaboration), Phys. Lett. B **805**, 135454 (2020)
- [13] S.V. Goloskokov and P. Kroll, Eur. Phys. J. A **47**, 112 (2011)
- [14] S.V. Goloskokov and P. Kroll, private communications, 2016
- [15] I. Bedlinsky et al. (CLAS Collaboration), Phys. Rev. C **90**, 025205 (2014)